

Influencing factors on Nano zero-valent iron colloid migration in porous media by coupling of CFD-DEM

Pengfei Liu¹, and Bate Bate²

¹Student, Zhejiang University, Hangzhou, China, email: 11812015@zju.edu.cn

²Professor, Zhejiang University, Hangzhou, China, email: BateBate@zju.edu.cn

ABSTRACT

Nano zero-valent iron (nZVI) injection technology, as a promising groundwater in-situ repair method for its high reactivity with pollutants in water, has been extensively studied in recent years. The stability of nZVI, especially its resistance to aggregation and the fluidity of the underground environment, are the key factors affecting its remediation efficiency. A numerical method of coupling computational fluid dynamics (CFD) with the discrete element method (DEM) was used to study nZVI colloid aggregation and clogging behavior. The surface energy density (SED) and particle charge were used to represent the Van der Waals force and Coulomb repulsion between the nZVI colloid, respectively. The retention mechanisms of nZVI in the soil matrix were investigated. The increase of Van der Waals force increases the agglomeration ability of the nZVI colloid. These agglomerates are more likely to be retained in the soil by the sieving and filtering action of the soil matrix. The increase in Coulomb repulsion leads to an increase in the energy barrier for nZVI agglomeration, which disperses nZVI in the soil pores and improves the mobility of nZVI. The increase in flow rate shortens the time of interaction between nZVI colloids, and at the same time increases the dragging force, which reduces the deposition efficiency of nZVI. The research further understands the aggregation and clogging behavior of nZVI under the ground and guides for improving the remediation efficiency.

Keywords: nZVI, van der Waals, Coulomb repulsion, CFD-DEM

1 INTRODUCTION

The nZVI is an effective in situ remediation for a wide variety of environmental contaminants (Ponder SM et al., 2000; Rangsvik et al., 2005; Zhu et al., 2009) for its flexible injection, strong reducibility, tiny size, and the ability to be surface coated (Wang et al., 2010; Crane et al., 2012; Huang et al., 2016). The remediation efficiency of contaminated sources is affected by the migration distance of nZVI and the dispersion of the nZVI in the contaminated zone. The nZVI tends to form agglomerates due to the attraction properties between nZVI such as magnetic properties or van der Waals force (Phenrat et al., 2006; Raychoudhury et al., 2012). These agglomerates are prone to form clogging and prevent the migration of nZVI in the soil matrix, reducing the nZVI content in the contamination source area (Phenrat et al., 2006; Chowdhury et al., 2012).

Factors affecting the mobility of nZVI particles include particle properties such as magnetic properties and environmental physicochemical conditions such as groundwater flow rate, ionic strength, and PH value (Phenrat et al., 2006; Kim et al., 2012; Busch et al., 2015; Torkzaban et al., 2015). The transport distance of bare nZVI in several types of porous media is only a few centimeters (Huang et al., 2016; Li et al., 2016). A lower pH value enhances the deposition (Kim et al., 2012). Higher nZVI particle concentrations contribute to more retention of nZVI and prefer to generate clogging causing an earlier particle breakthrough at the outlet (Bradford and Bettahar, 2006; Hosseini and Tosco, 2013; Strutz et al., 2016). The nZVI particles with higher injection velocity have lower retention, higher mobility, and more homogeneous distributions along the column (Strutz et al., 2016). Coating the nZVI surface with polymers such as polyacrylic acid or carboxymethyl cellulose was widely used to improve the mobility and stabilization of nZVI by providing repulsion (Schrack et al., 2004; He et al., 2007). Some polyelectrolytes were also added in colloidal solutions for avoiding aggregation by generating inter-particle repulsion to counter the attraction between particles (Raychoudhury et al., 2014).

In this study, a coupling of the CFD-DEM method was proposed to simulate the migration process of the nZVI colloid in the solid matrix. The van der Waals force was represented by surface energy density, and the Coulomb repulsion was calculated by particle charge. This study aimed to investigate the influencing factors of injection velocity, van der Waals force, and Coulomb repulsion on nZVI colloid migration and aggregation. The migration and aggregation trends were analyzed and visualized by numerical method.

2 METHOD AND MODEL

2.1 Numerical method

The Discrete element method following the Newton's second law was proposed by Cundall and Strack in 1979 (Cundall and Strack, 1979). The movement of a single particle is controlled by:

$$m_i \frac{d\vec{v}_i}{dt} = \sum_{j=1}^n \vec{F}_{ji} + \vec{g}_i + \vec{F}_e \quad (1)$$

$$I_i \frac{d\omega_i}{dt} = \sum_{j=1}^n (\vec{r}_{ij} \times \vec{F}_{ji}) + M_e \quad (2)$$

where m_i , \vec{v}_i , \vec{g}_i , I_i , and ω_i are the mass, velocity, gravity, rotational inertia, and angular velocity of the particle i , respectively. \vec{r}_{ij} is the vector of the center point of particle j pointing to the contact point. \vec{F}_e and M_e are the external force and the external torque, respectively. \vec{F}_{ji} is the contact force between particles i and j , which is calculated by the contact model using the explicit numerical scheme. The Hertz-Mindlin contact model combined with Johnson-Kendall-Roberts (JKR) contact model is used in this study. The van der Waals force between particles is calculated by the JKR model. The normal force F_{JKR} containing the JKR item is calculated by surface energy density γ and overlap δ :

$$F_{JKR} = -4\sqrt{\pi\gamma E^*} \alpha^{3/2} + \frac{4E^*}{3R^*} \alpha^3 \quad (3)$$

$$\delta = \frac{\alpha^2}{R^*} - \sqrt{4\pi\gamma\alpha/E^*} \quad (4)$$

where E^* and R^* are the equivalent modulus and radius of the two particles, respectively.

$$E^* = \left(\frac{1}{E_1} + \frac{1}{E_2} \right)^{-1} \quad (5)$$

$$R^* = \left(\frac{1}{R_1} + \frac{1}{R_2} \right)^{-1} \quad (6)$$

The normal damping force F_n^d is calculated by (Hertz, 1882):

$$F_n^d = -2\sqrt{5/6} \beta \sqrt{S_n m^* v_n^{rel}} \quad (7)$$

where v_n^{rel} is the normal relative velocity and

$$S_n = 2E^* \sqrt{R^* \delta_n} \quad (8)$$

where δ_n is normal overlap. The tangential force F_t and tangential damping force F_t^d are defined as follows (Mindlin, 1949; Mindlin & Deresiewicz, 1953):

$$F_t = -S_t \delta_t \quad (9)$$

$$S_t = 8G^* \sqrt{R^* \delta_n} \quad (10)$$

$$F_t^d = -2\sqrt{5/6} \beta \sqrt{S_t m^* v_t^{rel}} \quad (11)$$

where δ_t is the tangential overlap, S_t is tangential stiffness, and v_t^{rel} is tangential relative velocity. β is calculated by the coefficient of restitution e :

$$\beta = \frac{\ln e}{\sqrt{\ln^2 e + \pi^2}} \quad (12)$$

and G^* is the equivalent shear modulus of the two particles:

$$G^* = \left(\frac{1}{G_1} + \frac{1}{G_2} \right)^{-1} \quad (13)$$

The linear cohesion model was adopted to calculate the normal contact force between the particle and wall for improving the computational efficiency:

$$F = KA \quad (14)$$

where K is energy density and A is contact area. The Coulomb repulsion is calculated by:

$$F_{rep} = k_e \frac{|Q_1||Q_2|}{d^2} \quad (15)$$

where k_e is constant and $k_e \approx 8.988e9 \text{ N}\cdot\text{m}^2\cdot\text{C}^{-1}$. Q_1 and Q_2 are charges of particle 1 and particle 2. d is the center distance between particles.

The motion of the fluid phase is controlled by the mass conservation and momentum equations as follows:

$$\frac{\partial \rho}{\partial t} + \nabla \cdot \rho \vec{v} = S_m \quad (16)$$

$$\frac{\partial \rho}{\partial t} (\rho \vec{v}) + \nabla \cdot (\rho \vec{v} \vec{v}) = -\nabla P + \nabla \cdot (\bar{\tau}) + \rho \vec{g} + \vec{F} \quad (17)$$

where S_m is the additional mass source; ρ and \vec{v} are the fluid density and velocity, respectively; P and \vec{g} are the pressure and gravitational acceleration, respectively; \vec{F} is the external body force, and $\bar{\tau}$ is the stress tensor, which is defined by fluid velocity \vec{v} and viscosity μ :

$$\bar{\tau} = \mu \left[(\nabla \vec{v} + \nabla \vec{v}^T) - \frac{2}{3} \nabla \cdot \vec{v} I \right] \quad (18)$$

The drag force F_{Drag} between solid phase and fluid phase is defined as follows:

$$F_{Drag} = K_D (u - u_p) \quad (19)$$

where u_p and u are particle and fluid velocity, respectively. K_D is defined as follows:

$$K_D = \frac{18\mu C_D R_N}{d_p^2 24} \quad (20)$$

where μ is fluid dynamic viscosity, and R_N is relative Reynolds number:

$$R_N = \frac{\rho d_p |u_p - u|}{\mu} \quad (21)$$

where ρ and d_p are fluid density and particle diameter, respectively. The drag coefficient C_D is calculated as follows:

$$C_D = k_1 + \frac{k_2}{R_N} + \frac{k_3}{R_N^2} \quad (22)$$

where k_1 , k_2 , and k_3 are the coefficients related to the relative Reynolds number R_N (Table. 1).

Table 1. Drag coefficient equations

R_N	C_D
1–10	$29.1667/R_N - 3.8889/R_N^2 + 1.222$
10–100	$46.5/R_N - 116.67/R_N^2 + 0.6167$

CFD software ANSYS FLUENT 2019 R3 (Canonsburg, Pennsylvania, USA) and DEM software EDEM (Edinburgh, EH2 3NH, UK) are adopted to calculate the solid phase and fluid phase, respectively. The drag force, particle position, and momentum between the solid phase and fluid phase are exchanged by a coupling scheme through an application program interface provided by FLUENT and EDEM.

2.2 Computational domain setting

In FLUENT, the length, width, and height of the computational domain are 3.74 mm, 1.20 mm, and 0.05 mm, respectively. The computational domain contains eight complete cylinders and four half-cylinders, which is regarded as soil matrix. The distance between the centers of the cylinders is 0.6 mm, which corresponds to a porosity of 0.366 for the model. The mesh independence analysis was shown in Table 2. A total of 18408 Hexa-grid mesh with a size of 20 μm was adopted to ensure the accuracy of fluid calculation and the mesh volume larger than the particle volume. The no-slip boundary condition was applied on the cylinder, whereas the periodic boundary condition was adopted in the y-direction and z-direction. The inlet and outlet boundary conditions are constant velocity and pressure, respectively. The inlet velocity was set from 0.002 to 0.02 m/s. and the outlet pressure was set to zero.

Table 2. Mesh independence analysis

Mesh number	Inlet velocity (m/s)	Outlet velocity (m/s)	Error (%)
925	0.002	0.0023423	1.712
5536	0.002	0.0023346	1.673
18408	0.002	0.0019927	0.365
124425	0.002	0.0019999	0.005

In EDEM, the size of the computational domain is the same as in FLUENT. The particle diameter is set to 20 μm , which is regarded as the nZVI cluster. The surface energy density in the Hertz-Mindlin with JKR model between particles was set from 0.1 J/m² to 0.001 J/m². Particles are generated randomly at the injection surface, which is 0.3 mm away from the inlet. The key particle properties were shown in Table 3.

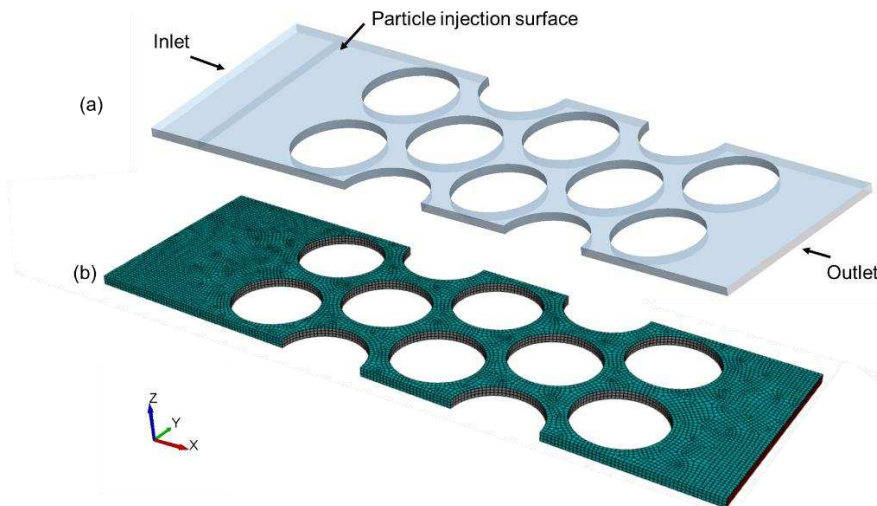


Figure 1. (a) Computational domain. (b) Model mesh

The EDEM simulation time step is set to 1e-7 s, which is 18% of the Rayleigh time step. The time step of FLUENT is set to 1e-5 s, which is 100 times of EDEM, and the total simulation time is controlled by FLUENT. The simulated case in this study took approximately 30-168 hours on a workstation with one Intel Core CPU (i9-9900K, 8 cores and 16 threads, 3.6GHz). It is worth noting that given the balance between computational accuracy and computer power efficiency, the method used in this study is an unsolved method that requires the fluid cell size to be larger than the particle.

Table 3. Key parameters of the simulation

Model parameter	value
Particle and wall	
Particle diameter (μm)	20
Particle mass density (kg/m^3)	2600
Particle shear modulus (Pa)	1e7
Particle Poisson ratio	0.25
Injection velocity (m/s)	0.002-0.02

Contact properties	
Coefficient of restitution	0.55
Coefficient of friction	0.8
Surface energy density (J/m ²)	0.001-0.1
Fluid properties	
Density (kg/m ³)	998.2
Viscosity (Pa·s)	0.001

3 RESULTS AND DISCUSSION

3.1 Validation of coupling program

The coupling program was validated by comparing the numerical results and theoretical solutions of a single sphere falling in the fluid under gravity. A rectangular container with a length, width, and height of 3 m, 3 m, and 6 m was used as the domain for the sphere to fall (Figure 2a). The diameter and the density of the sphere were set to 0.1 m and 2650 kg/m³, respectively. At the start of the simulation, the sphere was placed at the center of the top surface and the initial velocity was set to 0 m/s. The falling of a single particle in the fluid is subject to gravity, buoyancy, and drag forces. Based on Newton's second law, the equation of motion for a single particle is:

$$\frac{1}{6}\pi d_p^3 \rho_p \frac{\partial u_r}{\partial t} = \frac{1}{6}\pi d_p^3 (\rho_p - \rho)g - \frac{1}{8}\pi d_p^2 \rho C_d u_r^2 \quad (23)$$

where ρ_p is particle density, u_r is the relative velocity between particle and fluid, and C_d is calculated by (Zhao et al., 2014):

$$C_d = \frac{24}{R_N} (1 + 0.15 R_N^{0.681}) + \frac{0.407}{1 + 8710/R_N} \quad (24)$$

The first term of the right side of the equation. 23 is the combined force of gravity and buoyancy, and the second term is the drag force. The comparisons of the velocity and displacement in the direction of falling between simulation solutions and theoretical solutions are shown in Figure 2. Due to the drag force is controlled by the relative velocity between the fluid and the solid, the particle will fall at a constant velocity when gravity, buoyancy, and drag force are balanced (Figure. 2b). Both the velocity and displacement versus time show a good agreement with theoretical solutions. The CFD-DEM coupling program is verified.

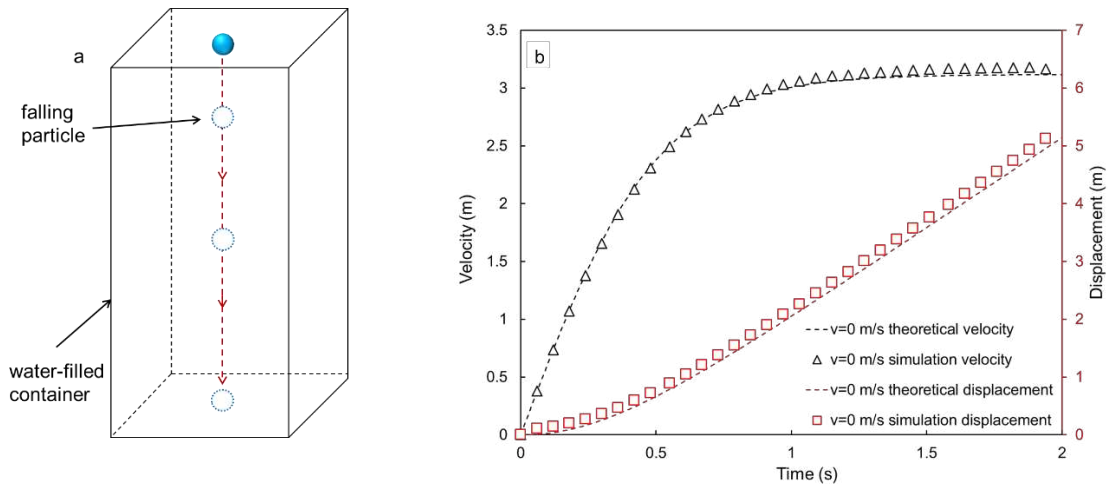


Figure 2. (a) Schematic diagram of a single particle falling in a water-filled container. (b) Velocity and displacement in the direction of falling versus time

3.2 Effects of Coulomb repulsion

The coulomb repulsion between particles is changed by varying the amount of charge of the particles. The three cases had the same injection velocity and SED, which were 0.002 m/s and 0.1 J/m², respectively. The charge in the three cases was 1e-15 C, 5e-15 C, and 1e-14 C. The mass of the particles inside the model decreases as the number of charges increases (Figure 3a). Case 2 and case 3 reach dynamic equilibrium after 0.6 s. The distribution of particles inside the model is shown in Figure 3b-3d. In case 1, clogging was generated at the model entrance. These clogging prevented the particles from continuing to migrate inside the model, resulting in a lower particle concentration behind the model (Figure 3b). In cases 2 and 3, no clogging was produced but agglomerates were generated. The size and number of agglomerates decrease with increasing particle charge. The increase in Coulomb repulsion raises the energy barrier to particle agglomeration, which requires greater attraction to form agglomerates. Consequently, the greater the Coulomb repulsion, the more uniform the distribution of particles in the model. This indicated that the dispersion and transport distance of nZVI can be improved by adding stabilizers that provide repulsion, such as carboxymethyl cellulose (CMC). When CMC is added to the nZVI solution, the CMC molecules will adsorb on the surface of the particles to provide a layer of negative charge, forming repulsion to prevent the particles from aggregating (He & Zhao, 2007).

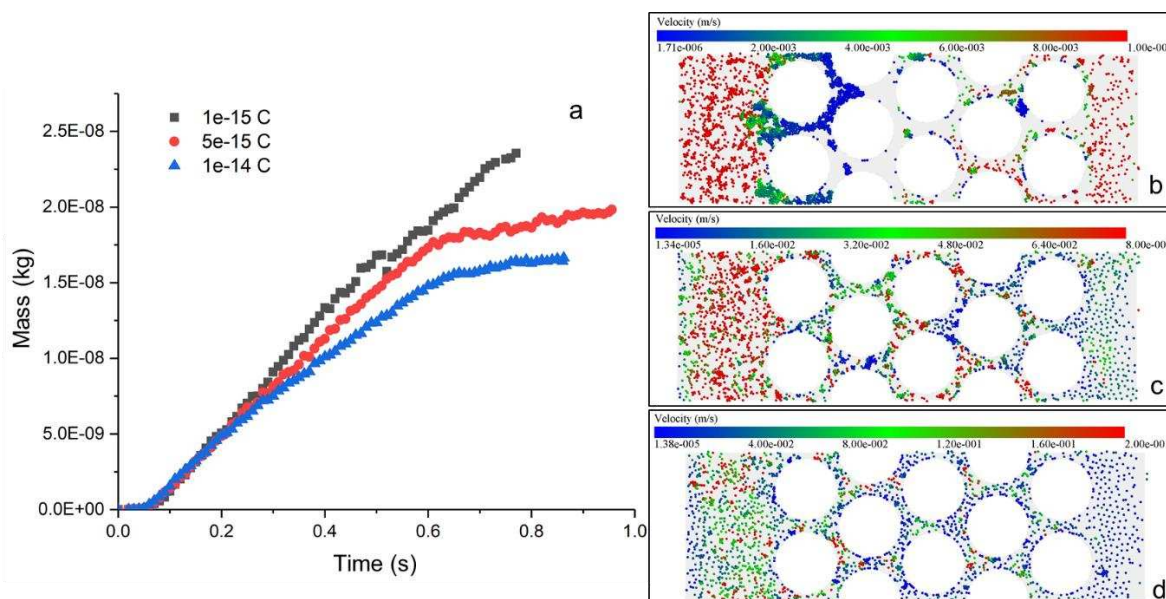


Figure 3. (a) Particle mass in model versus time under different particle charges. (b) Case 1: particle charge = 1e-15 C. (c) Case 2: particle charge = 5e-15 C. (d) Case 3: particle charge = 1e-14 C

3.3 Effects of injection velocity

The injection velocity was increased from 0.002 m/s to 0.02 m/s on the base of Case 3. The particle distribution in the pores is shown in Figure 4. The higher the injection velocity, the earlier the particle mass distribution within the model reaches equilibrium, indicating that nZVI particles remain in the model for a shorter time (Figure 4a). The equilibrium mass value decreases as the injection velocity increases. At high injection velocity, particle concentrations in the pores are lower than that at low injection velocity (Figure 4b-4d). A lower concentration reduces the probability of collisions between particles, which in turn reduces the chance of forming agglomerates. Consequently, high injection velocity enhances the migration distance of nZVI particles and reduces agglomerate formation. Previous studies showed that higher injection velocity increases the number of movable particles by 5-25% compared to lower injection velocity (Strutz et al. 2016). It is worth noting that although increasing the injection velocity can improve the transport distance and reduce the formation of agglomerates, a small number of agglomerates still appear in the pores (Figure 4d). These agglomerates require the addition of stabilizers to increase the repulsion between nZVI particles or to reduce the nZVI particle attraction.

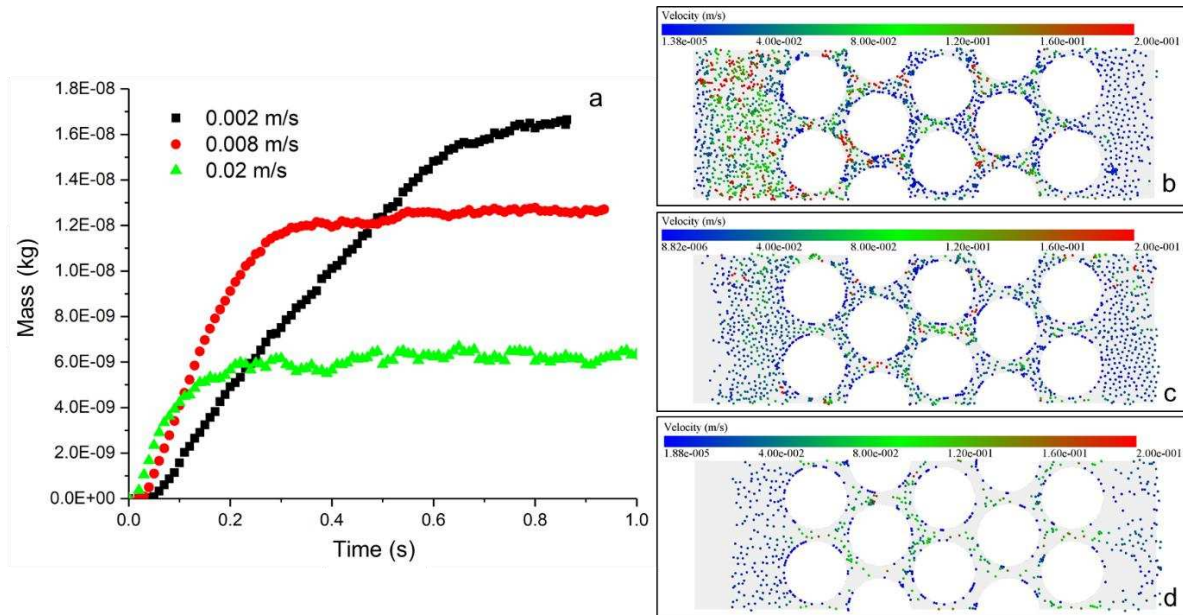


Figure 4. (a) Particle mass in model versus time under different injection velocities. (b) Case 4: injection velocity = 0.002 m/s. (c) Case 5: injection velocity = 0.008 m/s. (d) Case 6: injection velocity = 0.02 m/s

3.4 Effects of van der Waals force

Keeping the injection velocity and charge constantly in case 6, the van der Waals force was reduced by decreasing the SED from 0.1 J/m² to 0.001 J/m². After 0.25 s, the particle masses in both cases reached equilibrium (Figure 5a). The lower the surface energy density, the higher the mass of particles distributed inside the model. When the surface energy density is reduced, the particle agglomerates inside the model are reduced and the particles are more uniformly distributed (Figure 5b-5c). Compared to case 8, a small number of small-size agglomerates formed in case 7, which was not sufficient to form clogging (Figure 5b). These small-sized agglomerates have greater inertia than individual nZVI particles, which makes them less prone to attach to the soil matrix (cylinders), causing fewer particles distributed in soil when SED is high.

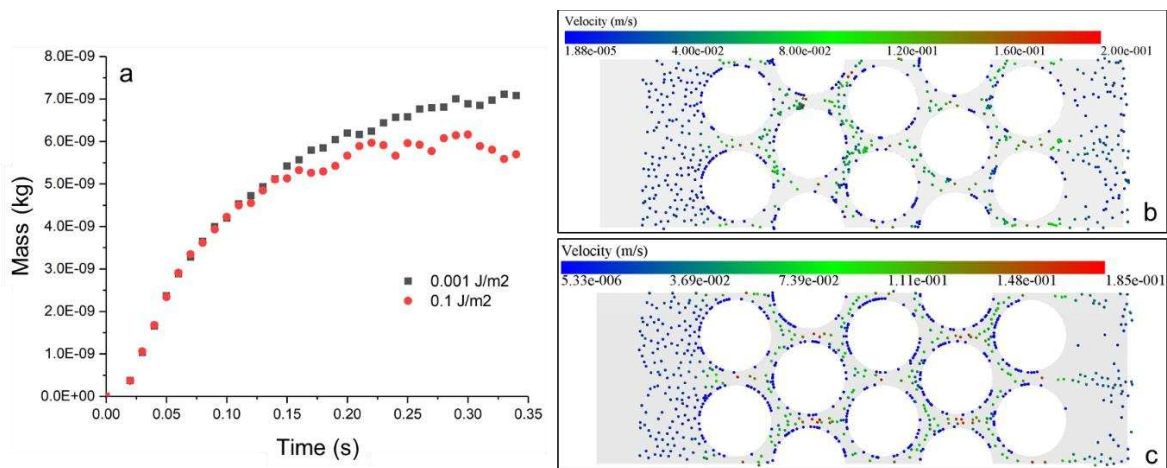


Figure 5. (a) Particle mass in model versus time under different SED. (b) Case 7: SED = 0.1 J/m². (c) Case 8: SED = 0.001 J/m²

4 CONCLUSIONS

The migration of nZVI in a homogeneous soil matrix was investigated by a CFD-DEM coupling method. The van der Waals and Coulomb repulsion forces between particles are adjusted by varying the SED

and particle charge. The van der Waals force, Coulomb repulsion, and injection velocity were changed, and their effects on nZVI particle migration and dispersion in the soil matrix were assessed and visualized. This study demonstrates the potential of CFD-DEM methods to quantitatively study the nZVI migration. The migration process and retention form of nZVI particles are visualized. The migration and clogging properties of the particles can be determined by the fundamental inter-particle force relationships. The present study was limited to the migration of nZVI particles in a homogeneous soil structure and the fluid loaded with nZVI particles was water. The heterogeneity of soil structure and the rheological properties of fluids should be considered in future studies.

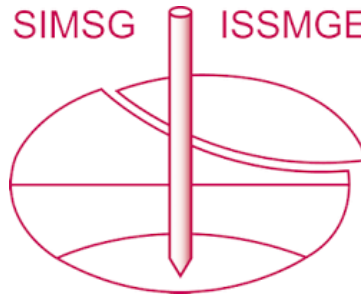
- (1) Coulomb repulsion prevents the formation of large-sized aggregates between nZVI particles, which tends to form clogging at the pore throat and prevent the particles from transporting to the target area. Consequently, coating nZVI with polymers such as polyacrylic acid or carboxymethyl cellulose, which provide repulsion between nZVI particles, can improve the dispersion and the transport distance of nZVI colloid.
- (2) In the case of the same nZVI particle mass, the increase in injection velocity reduces the concentration of nZVI particles in the pores, and these particles are less prone to collision. High injection velocity contributes to the effective delivery of nZVI in the soil matrix and transport to the target zone.
- (3) The van der Waals force between nZVI particles promotes the formation of agglomerates and reduces the transport capacity and dispersion of nZVI colloid. At high flow velocity (0.02 m/s), the concentration of nZVI particles in the soil matrix with high SED (0.1 J/m²) is lower than that of low SED (0.001 J/m²).

REFERENCES

- Bradford, S. A., & Bettahar, M. (2006). Concentration dependent transport of colloids in saturated porous media. *Journal of Contaminant Hydrology*, 82(1), 99-117.
- Busch, J., Meißner, T., Potthoff, A., Bleyl, S., Georgi, A., Mackenzie, K., Trabitzzsch, R., Werban, U., & Oswald, S. (2015). A field investigation on transport of carbon-supported nanoscale zero-valent iron (nZVI) in groundwater. *Journal of Contaminant Hydrology*, 181, 59-68.
- Chowdhury, A. I., O'Carroll, D. M., Xu, Y., & Sleep, B. E. (2012). Electrophoresis enhanced transport of nano-scale zero valent iron. *Advances in Water Resources*, 40, 71-82.
- Crane, R., & Scott, T. (2012). Nanoscale zero-valent iron: Future prospects for an emerging water treatment technology. *Journal of Hazardous Materials*, 211, 112-125.
- Cundall, P. A., & Strack, O. D. L. (1979). A discrete numerical model for granular assemblies. *Géotechnique*, 29(1), 47-65.
- He, F., & Zhao, D. (2007). Manipulating the Size and Dispersibility of Zerovalent Iron Nanoparticles by Use of Carboxymethyl Cellulose Stabilizers. *Environmental Science & Technology*, 41(17), 6216-6221.
- Hertz, H (1882) On the contact of elastic solids. *J reine und angewandte Mathematik* 92:156–171
- Hosseini, S. M., & Tosco, T. (2013). Transport and retention of high concentrated nano-Fe/Cu particles through highly flow-rated packed sand column. *Water Research*, 47(1), 326-338.
- Huang, L., Liu, Q., Zhou, S., Xue, J., & Liu, G. (2016). Laboratory investigation of a magnetic system used for enhancing the migration of nanoscale zero-valent iron (NZVI). *Journal of the Taiwan Institute of Chemical Engineers*, 61, 205-210.
- Kim, H.-J., Phenrat, T., Tilton, R. D., & Lowry, G. V. (2012). Effect of kaolinite, silica fines and pH on transport of polymer-modified zero valent iron nano-particles in heterogeneous porous media. *Journal of Colloid and Interface Science*, 370(1), 1-10.
- Li, J., Rajajayavel, S. R. C., & Ghoshal, S. (2016). Transport of carboxymethyl cellulose-coated zerovalent iron nanoparticles in a sand tank: Effects of sand grain size, nanoparticle concentration and injection velocity. *Chemosphere*, 150, 8-16.
- Mindlin, R. D. (1949). Compliance of Elastic Bodies in Contact. *Journal of Applied Mechanics*, 16(3), 259-268.
- Mindlin, R. D., & Deresiewicz, H. (1953). Elastic Spheres in Contact Under Varying Oblique Forces. *Journal of Applied Mechanics*, 20(3), 327-344. <https://doi.org/10.1115/1.4010702>
- Phenrat, T., Saleh, N., Sirk, K., Tilton, R. D., & Lowry, G. V. (2006). Aggregation and Sedimentation of Aqueous Nanoscale Zerovalent Iron Dispersions. *Environmental Science & Technology*, 41(1), 284-290.

- Ponder, S. M., Darab, J. G., & Mallouk, T. E. (2000). Remediation of Cr(VI) and Pb(II) Aqueous Solutions Using Supported, Nanoscale Zero-valent Iron. *Environmental Science & Technology*, 34(12), 2564-2569.
- Rangsivek, R., & Jekel, M. (2005). Removal of dissolved metals by zero-valent iron (ZVI): Kinetics, equilibria, processes and implications for stormwater runoff treatment. *Water Research*, 39(17), 4153-4163.
- Raychoudhury, T., Tufenkji, N., & Ghoshal, S. (2012). Aggregation and deposition kinetics of carboxymethyl cellulose-modified zero-valent iron nanoparticles in porous media. *Water Research*, 46(6), 1735-1744.
- Raychoudhury, T., Tufenkji, N., & Ghoshal, S. (2014). Straining of polyelectrolyte-stabilized nanoscale zero valent iron particles during transport through granular porous media. *Water Research*, 50, 80-89.
- Schrick, B., Hydutsky, B. W., Blough, J. L., & Mallouk, T. E. (2004). Delivery Vehicles for Zerovalent Metal Nanoparticles in Soil and Groundwater. *Chemistry of Materials*, 16(11), 2187-2193.
- Strutz, T. J., Hornbruch, G., Dahmke, A., & Köber, R. (2016). Effect of injection velocity and particle concentration on transport of nanoscale zero-valent iron and hydraulic conductivity in saturated porous media. *Journal of Contaminant Hydrology*, 191, 54-65.
- Torkzaban, S., Bradford, S. A., Vanderzalm, J. L., Patterson, B. M., Harris, B., & Prommer, H. (2015). Colloid release and clogging in porous media: Effects of solution ionic strength and flow velocity. *Journal of Contaminant Hydrology*, 181, 161-171.
- Wang, Q., Qian, H., Yang, Y., Zhang, Z., Naman, C., & Xu, X. (2010). Reduction of hexavalent chromium by carboxymethyl cellulose-stabilized zero-valent iron nanoparticles. *Journal of Contaminant Hydrology*, 114(1), 35-42.
- Zhao, T., Houlsby, G. T., & Utili, S. (2014). Investigation of granular batch sedimentation via DEM–CFD coupling. *Granular Matter*, 16(6), 921–932.
- Zhu, H., Jia, Y., Wu, X., & Wang, H. (2009). Removal of arsenic from water by supported nano zero-valent iron on activated carbon. *Journal of Hazardous Materials*, 172(2), 1591-1596.

INTERNATIONAL SOCIETY FOR SOIL MECHANICS AND GEOTECHNICAL ENGINEERING



This paper was downloaded from the Online Library of the International Society for Soil Mechanics and Geotechnical Engineering (ISSMGE). The library is available here:

<https://www.issmge.org/publications/online-library>

This is an open-access database that archives thousands of papers published under the Auspices of the ISSMGE and maintained by the Innovation and Development Committee of ISSMGE.

The paper was published in the proceedings of the 9th International Congress on Environmental Geotechnics (9ICEG), Volume 4, and was edited by Tugce Baser, Arvin Farid, Xunchang Fei and Dimitrios Zekkos. The conference was held from June 25th to June 28th 2023 in Chania, Crete, Greece.